3D printing of magnetostrictive property in 17/4 ph stainless steel

N. Ahmed, R. Deffley, B. Kundys, N.A. Morley

3D printing of magnetostrictive property in 17/4 ph stainless steel

N. Ahmed[1], R. Deffley[1,2], B. Kundys[3] and N. A. Morley[1]

1. Department of Materials Science and Engineering, University of Sheffield, Sheffield, S1 3JD, UK

2. Royce Translational Centre, Sheffield Business Park, Europa Ave, Tinsley, Sheffield, S9 1ZA, UK

3. Université de Strasbourg, CNRS, Institut de Physique et Chimie des Matériaux de Strasbourg (IPCMS), UMR 7504, 23 rue du Loess, Strasbourg, 67034, France

1. Abstract

Additive manufacturing (AM) of metallic alloys significantly advances diverse areas of science/engineering with a prosperous future trend. Although this technology is also very attractive for smart materials development, the creation of a pre-programmed "4th dimension" property to appear in response to external stimuli represents an important challenge. Here we report on 3D printing of stainless steel based magnetic alloy and detail the ways to optimize the magnetisation and magnetostriction to be used for actuation and sensing. By controlling the printing parameters and sintering process, we are able to tune the magnetic and magnetoelastic properties of the 17/4 ph stainless steel, demonstrating material fabrication multi-function with a cost effective advantage. The stainless steel 17/4 ph samples in the as-printed (AP) and sintered steel (SS) stages are compared. In the developed SS sample, a remarkable increase of 18% in saturation magnetisation yet with 12.6 % lower coercivity was achieved. Moreover, the 54% higher magnetostriction was developed for the SS sample compared to the AP sample. Plus, the difference in anisotropy energy K^1 was also lower for the SS sample. The structural and magnetic properties control are reported at each stage of the printing process, demonstrating development and optimization prospects of 3D printable metallic sensors and actuators.

Keywords: Magnetostriction, Stainless steel 17/4 ph, 3D printing, extrusion, desktop metal bound deposition

Corresponding Author: Nisar Ahmed, nahmed7@sheffield.ac.uk

1 Introduction

There has been a sharp interest in 3D printing of magnetic materials in recent years. In particular, additive manufacturing (AM) allows tuneable designs that can improve the material's performance and reduce waste, thus increasing the efficiency [1]–[7]. 3D printing has been of interest in most manufacturing industries as well as the internet of things, this includes exploiting the benefits from using AM magnetic materials as shown in [8]–[14]. Another important inherent property of magnetic materials is the magnetostriction effect, also known as the magnetoelastic effect. The magnetostriction effect has been used in applications such as energy harvesters, sensors and actuators [15], [16], [25], [17]–[24]. For example, one use of magneto-active materials was as a magnetoelectric antenna, which was designed and used for wireless energy harvesting and in sensing devices as published in [26], [27]. In [28], they have printed a low-cost environmentally friendly wireless device for smart electronics and have improved induction efficiency by 94% using magnetic core. The two main forms of magnetoelastic effects [29] can be described by Eq. 1: Joule magnetostriction, where the material changes in length under a magnetic field and Eq. 2: Inverse-Joule or Villari Effect, where the magnetic flux density changes direction under an applied strain.

$$\varepsilon = \sigma \, / \, E_y^H + d_{33} H \qquad (1)$$

$$B = d_{33}\sigma + \mu^{\sigma} H \qquad (2)$$

Where in Eq. 1, ε is the strain, σ is stress, E_y^H is the compliance coefficient at constant field strength and $d_{33} = d\varepsilon/dH$ (strain/Field). Where in Eq. 2, B is the magnetic flux density in Tesla (T), $d_{33} = dB/d\sigma$ (induction/stress) which is the magnetostrictive constant, μ^{σ} is the permeability at constant mechanical stress and H is the magnetic field. The magnetic flux density, B is related to the magnetisation of the material, M by: $B = \mu_0 (M + H)$, where μ_0 is the relative permeability.

Currently, the classical magnetostrictive materials are: FeCo, FeSiB, FeGa (Galfenol) and Terfenol-D. These are traditionally produced either by arc-melting or melt-spinning, which limits the design. However, with the development of 3D metallic printing technology, fabrication of more complex designs and shapes has become possible. With the recent rise of new materials fabrication procedures, a vast set of strategies for alloy-property engineering is now available. However understanding how particular printing parameters influence magnetic and magnetoelastic properties remains an important challenge [18], [30]–[35]. In particular, the application potential of magnetostriction in functional amorphous and nanocrystalline magnetic materials (ferrites and amorphous alloys) has attracted a lot of attention due to lower cost and lower coercivity along with higher saturation magnetostriction as seen in Fig.1. In Fig. 1, the solid line represents the trade off point to filter and select a material. For example, in Fig. 1b, low coercivity and high magnetostriction are desired therefore the slope is set as 1 as both properties are equally as important. If the price of the material is not critical to an application, then the slope of the line can be adjusted accordingly.

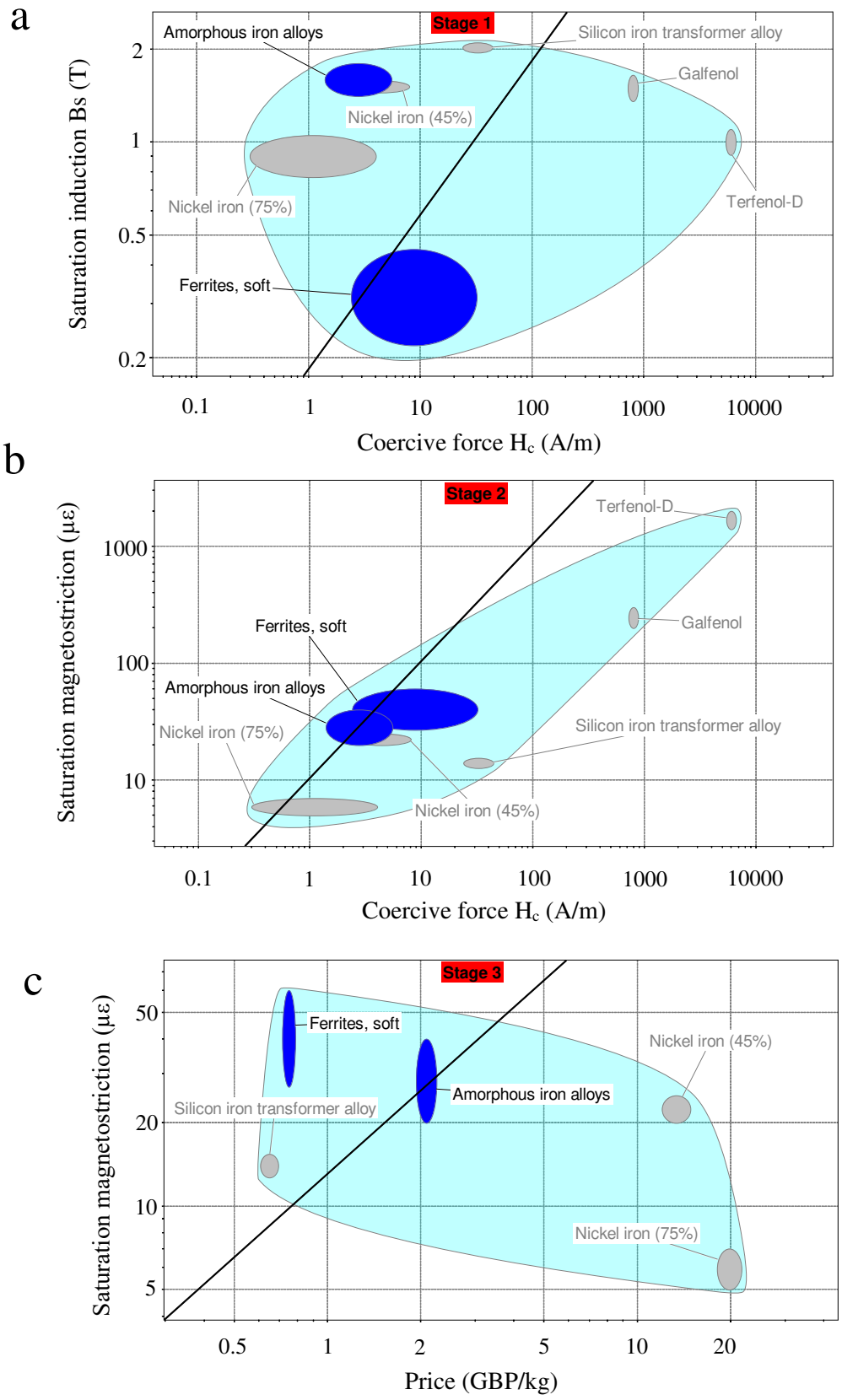

Fig. 1. (a) Stage 1- saturation magnetisation vs coercive force, (b) Stage 2- Saturation magnetostriction vs coercive force and (c) Stage 3-Saturation magnetostriction vs Price of functional materials taken from Ansys grantaedupack 2021 R2 material selection database (Ashby chart)

To remove the issues that arise due to the production of magnetostrictive powders, printing has been achieved by the extrusion method i.e. fused deposition modelling (FDM). The feedstock is made by mixing the magnetic material such as stainless steel 17/4 ph with a polymer binder into a paste via a moulding process. However, the disadvantage is that the polymer binder needs to be removed and may affect the design capability and performance of the magnetic material. Therefore, the green body requires further heat treatment such as sintering for densification of the structure. Thus understanding how this simpler process changes the magnetic properties of the magnetostrictive material is important. Here we investigate the structural and magnetic properties, including the magnetostriction of stainless steel 17/4 ph, to determine how the 3D printing process and sample design modifies these properties.

2 Experimental Methods

The samples were designed and printed via desktop metal bound disposition (DMBD) at the Royce Translational Centre (part of the Henry Royce Institute) at the University of Sheffield. Stainless steel 17/4 ph soft magnetic material was selected and used to print structures in this paper. The As-received (AR) feedstock is in the form of pre-mixed rods consisting of binder and metal powder. Fig. 2a, shows where the AR was heated and fed by mechanical extrusion onto the base to produce the sample design, this is known as As-printed (AP). The debinding process Fig. 2b was done in two stages: solvent and drying. Once dried, the sample is placed into the furnace for sintering as seen in Fig. 2c, under an inert atmosphere of argon-2.8% Hydrogen and at a temperature close to the melting point.

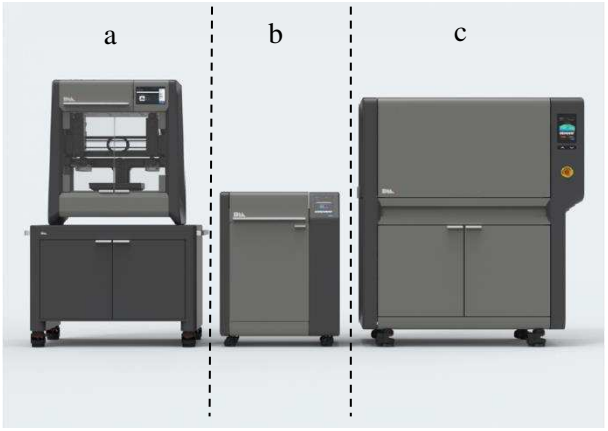

Fig. 2. Studio system consist of (a) DMBD printer, (b) debinder and (c) furnace

The final sample produced is a sintered, fully-dense stainless steel (SS) containing no polymer. Steps for thermal debinding and sintering in the furnace are presented in table 1 [36].

Table 1. Procedure for heat treatment, sintering and cooling for DMBD printer [36]

Steps	Temperature Range	Time	Ramp Rate
1	50 ➡ 160 °C	Over: 120 min Hold: 90 min	0.91°C per minute
2	160 ➡ 260 °C	Over: 300 min Hold: 180 min	0.33°C per minute
3	260 ➡ 600 °C	Over: 114 min Hold: 240 min	3°C per minute
4	600 ➡ 1340 °C	Over: 247 min Hold: 120 min	3°C per minute
5	Cooling	Until room temperature	Max

The Fourier transform infrared by attenuated total reflection (FT-IR ATR) technique was used to identify the polymer. The scanning electron microscope (SEM) FEI inspect F50 was used to image the samples, along with determining the composition using EDS and Oxford Instrument AZtecOne software. The hysteresis loops of each sample were measured using a Quantum Design MPMS-3 SQUID magnetometer up to 1200 kA/m. The demagnetising field of the desktop prints were measured using a magnetic camera (Magcam) with a resolution of 0.1 mm^2. The Magcam contains 1000 Hall sensors that measure the change in magnetic flux density providing a 2D magnetic image of the sample. The magnetostriction was measured by the change in resistance of a strain gauge (gauge factor of 2.1), as shown in Eq. 3. This can be rearranged to give Eq. 4 to calculate the strain, and hence the magnetostriction constant, ($\lambda = \varepsilon$), where R is resistance, G is the gauge factor of the strain gauge and L is the length of the sample. An Agilent E4980A from IPCMS was used to record the resistance of the strain gauge while 2 V DC bias was applied at a 100 kHz frequency.

$$\frac{\Delta R}{R} = G\frac{\Delta l}{l} \tag{3}$$

$$\varepsilon = \frac{\Delta R}{RG} \tag{4}$$

Fig. 3 shows the experimental set up for measuring Joule magnetostriction. The strain gauge was fixed to the sample by cyanoacrylate glue. The strain gauge was mounted on the side of all the printed stainless steel. Field direction was either in a parallel or perpendicular direction to the layers, achieved by adjusting the electromagnet position.

a

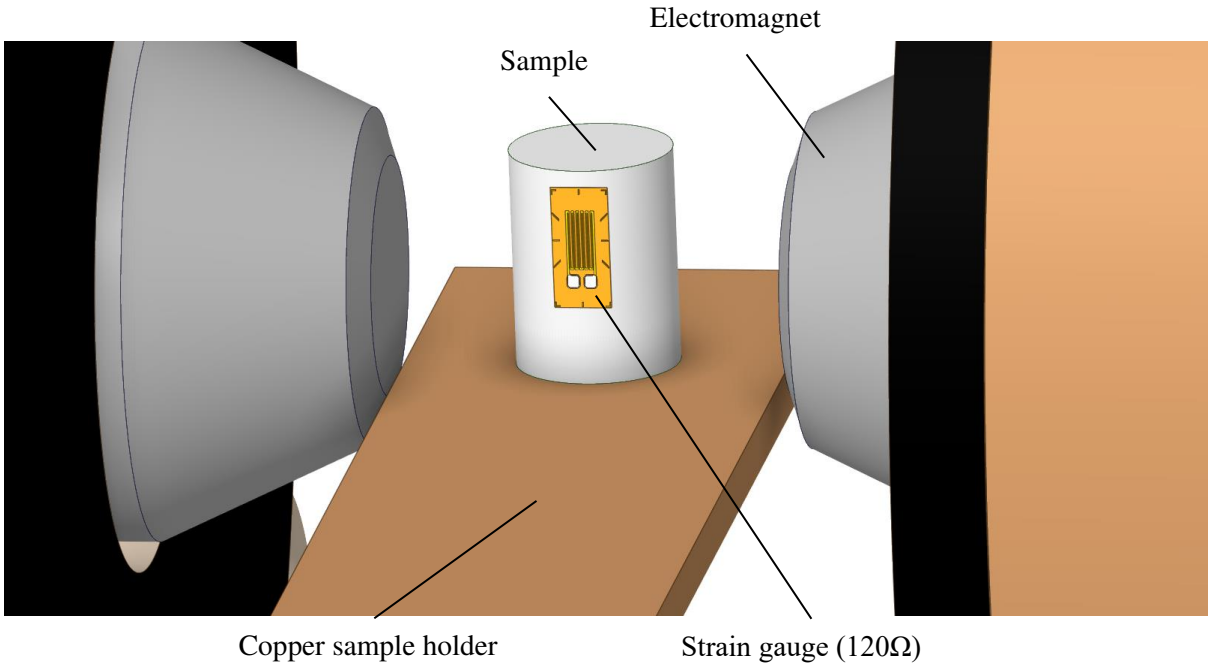

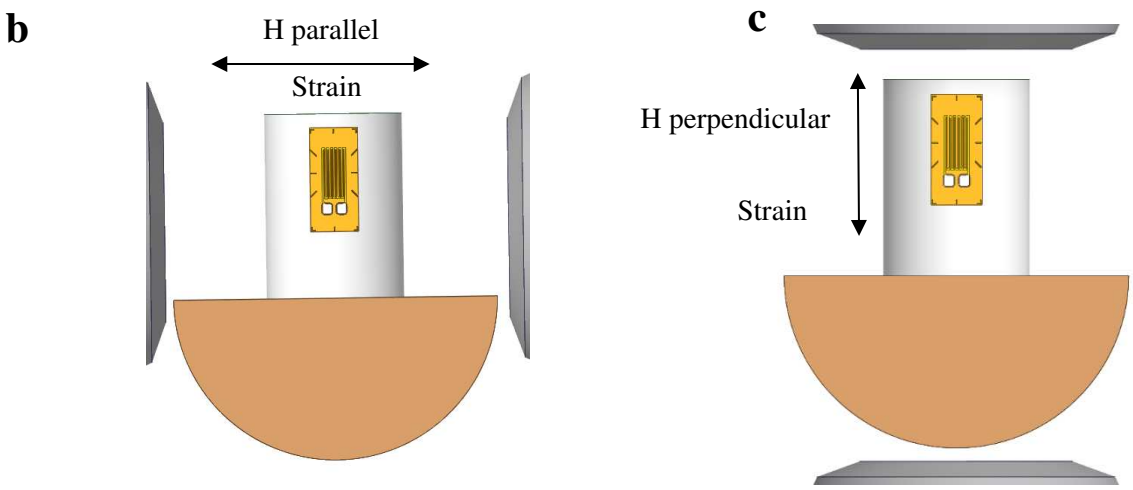

Fig. 3. (a) Magnetostriction measurement schematic showing (b) parallel and (c) perpendicular configuration of the experiment with respect to magnetic field (H) and strain (not to scale)

3 3D printed grid designs

A set of grids (Fig. 4), were printed by the DMBD and sintered, with print size of 30 x 30 mm, for different track gaps of (a) 2 mm, (b) 4 mm and (c) 6 mm and height of 2 mm. The sintered grid structure underwent shrinkage with a rate of 16.6% therefore the final dimensions of the track gaps were (d) 1.5, (e) 3 and (f) 5 mm respectively. The track gap represents the infill size of the printed grid design. Therefore, this paper will explore how magnetic and structural are affected in different stages of printing and infill sizes.

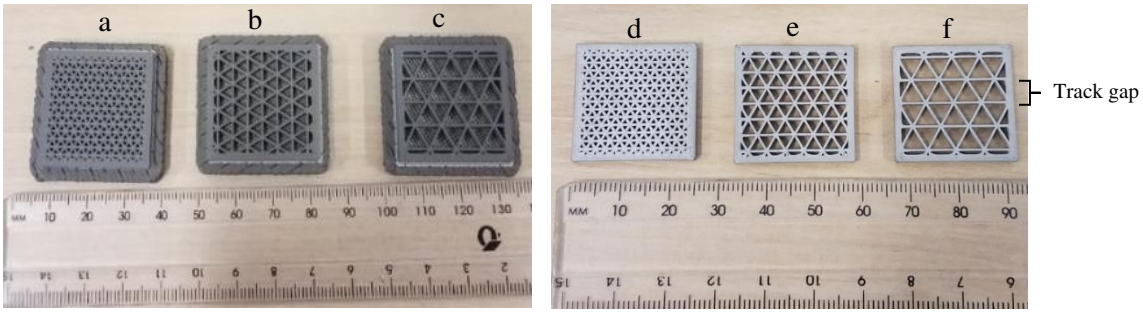

Fig 4. DMBD print AP samples showing different track length of (a) 2 mm, (b) 4 mm and (c) 6 mm and SS samples showing different track length of (d) 1.5 mm, (e) 3 mm and (f) 5 mm

4 Results and discussion

4.1 Physical and structural characterisation

From the FTIR results (Fig. 5), the polymer was identified to be polypropylene (PP) in the AR and AP sample. The spectra for the AR and AP samples look almost identical except for the percentage transmittance. For both the AR and AP samples, there are absorption peaks at 2950 cm^{-1}, 2915 cm^{-1} and 2847.91 cm^{-1}, which suggest that the sample has a C-H_n functional group, similar to the polypropylene published values [37]. The peak at 1738 cm^{-1} is not from the polypropylene spectra, which suggest that this may be a mixture of polymers as the peak is from a C=O stretch, which from the literature suggests that the functional group C=O, closely resembles PETE. However, PETE does not contain C-H_n group

therefore the FT-IR spectra matches the spectra for PP. The transmittance decreases as the wavenumber (cm^{-1}) decreases, which is due to reflection from the sample, as stainless steel has a high reflectivity.

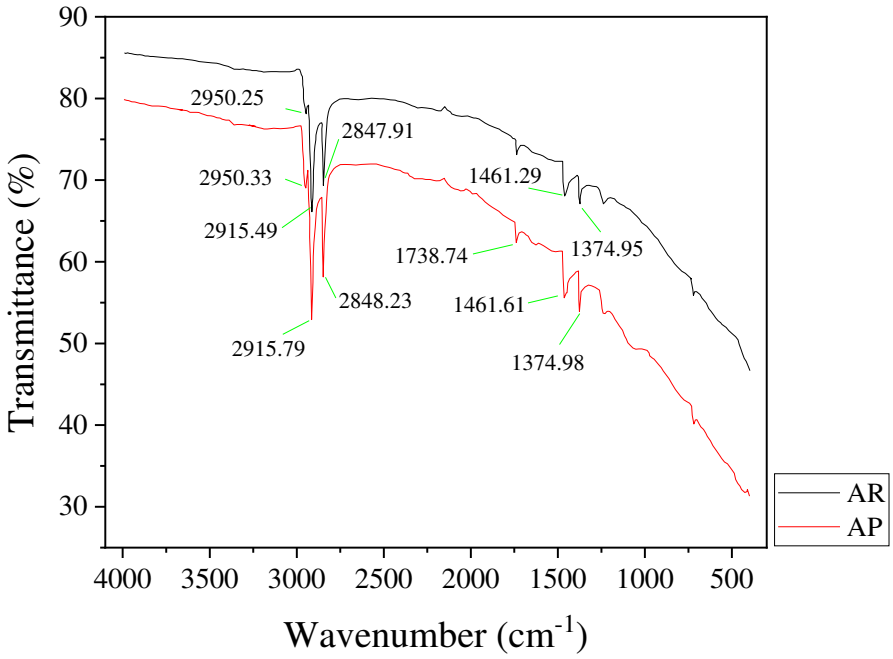

Fig. 5. FT-IR spectrum transmittance and wavelength of AR (black) and AP (red) samples- colour should be included

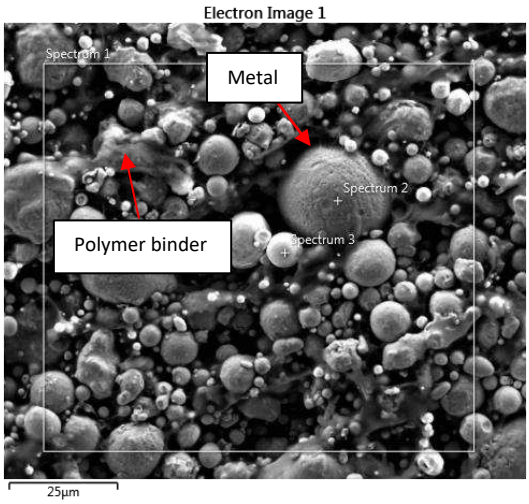

Fig. 6. AR sample SEM image showing polymer binder and metal sites

Fig. 6 shows for the AR sample, that metal particles observed are a large spherical-shape with a diameter of 25 µm and below. The polymer binder can be seen as non-spherical shapes due to the fibrous nature of the binder. Therefore, the polymer binder holds the metal together by adhesion and restricting the movement of the metal particles, loosely holding the structure together.

Fig. 7 shows the SEM, element map and composition of the AR, AP and SS samples in (a), (b), (c), (d), (e) and (f), with the weight percentage of the absolute measurement given in Table 2. The elements were measured at multiple locations as seen in (c) and (e), with an average value being calculated. Areas that contained porosity were excluded therefore only metallic/polymer areas were selected. In (c) the

polymer and metallic elements in the AP sample were not uniform across the sample therefore more points were required to provide a better average of the elements. The EDS map in (b) shows iron and chromium elements loosely bonded with impurities of copper and oxygen. The EDS mapping in (d) shows the expected weight percent for the elements iron and chromium are present for the AP steel, whereas oxygen and silicon are either impurities or air gaps within the structure. This matches the supplier's element composition for stainless steel 17/4 ph[38]. For the SS sample, the EDS map shows that there is a notable increase in iron as the iron is homogeneous across the sample. In (e), the SEM image shows the boundaries are homogenous and crystallised as the air is removed. In the AR and AP samples EDS maps, the iron is localised in the metal/polymer mixture. This could mean that the magnetisation would be higher in the SS sample but with an isotropic magnetisation direction.

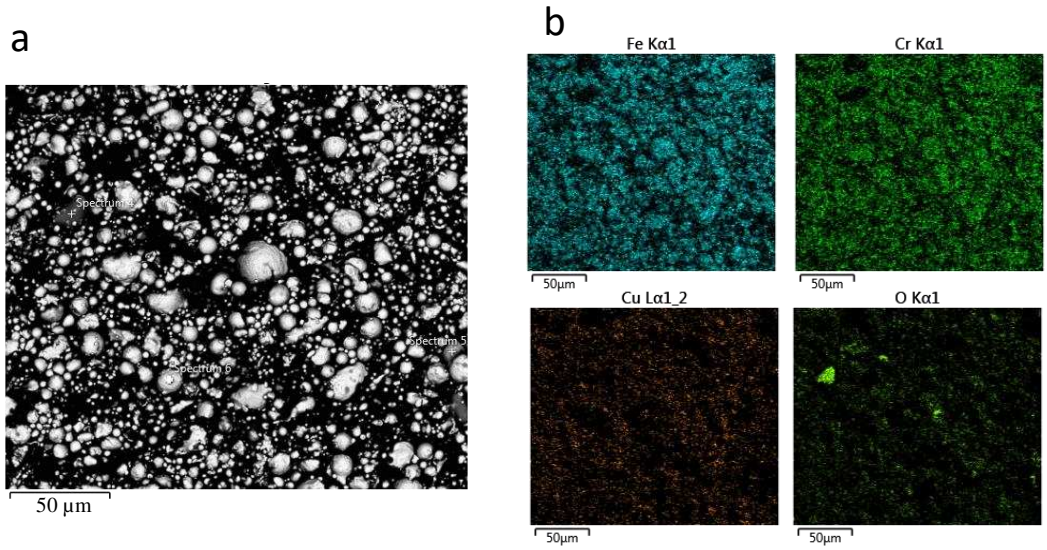

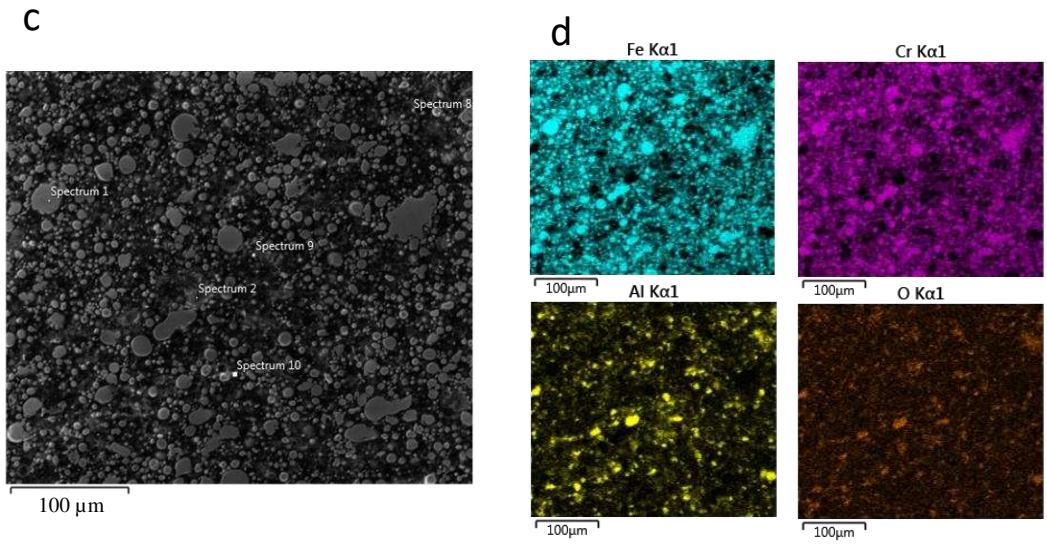

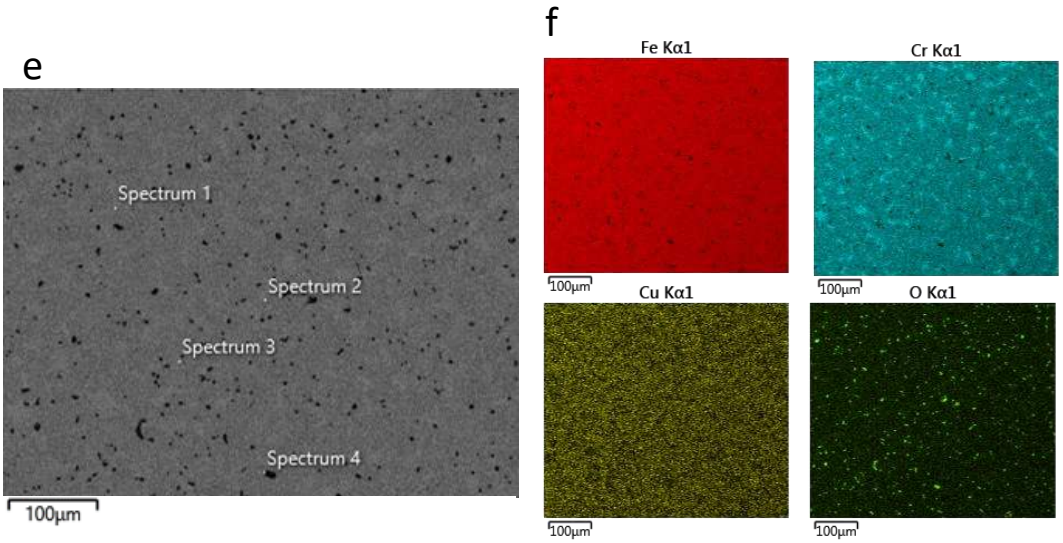

Fig. 7. AR structure (a) SEM and (b) EDS map, AP structure (c) SEM and (d) EDS map and SS structure (e) SEM and (f) EDS map - colour should be included

Table 2 Percentage of elements from the EDS spectrum of AR, AP and SS samples

Elements	**AR**	**AP**	**SS**
Fe	71 ± 3	64 ± 3	74 ± 1
Cr	17 ± 2	16 ± 1	17 ± 1
C	<1 ± 0.01	<1 ± 0.01	<1 ± 0.01
Cu	4 ± 1	3 ± 1	3 ± 1
Si	1 ± 0.2	1 ± 0.1	1 ± 0.1
O	2 ± 0.4	1 ± 0.3	1 ± 0.3
Al	<1 ± 0.1	10 ± 2	<1 ± 0.1
Ni	2 ± 1	1 ± 1	2 ± 1

4.2 Magnetisation

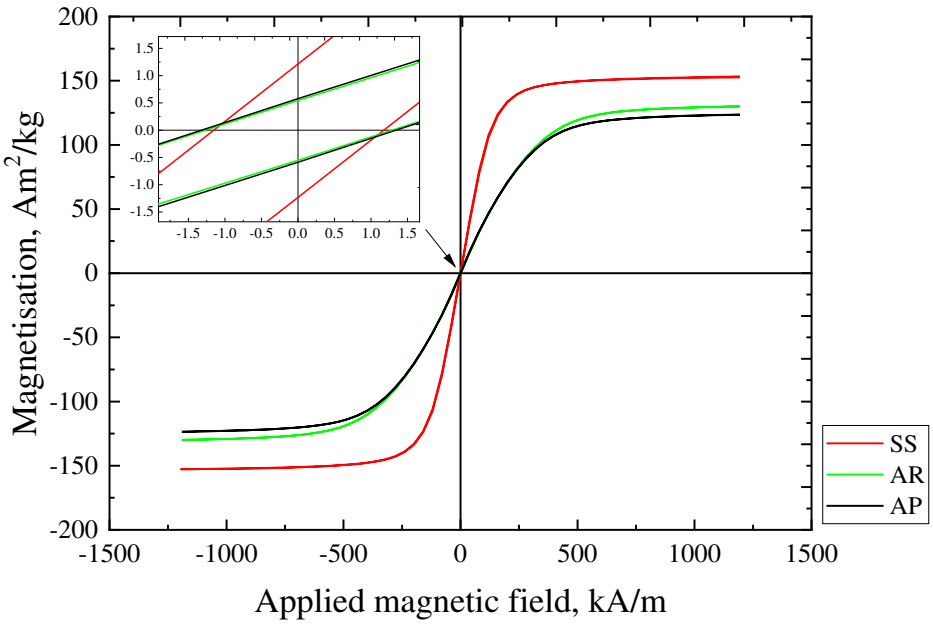

Fig. 8. SQUID hysteresis loop of AR, AP and SS samples where coercivity, remanence and saturation magnetisation is observed - colour should be included

Fig. 8 shows the hysteresis loops for the AR, AP and SS samples which shows soft ferromagnetic behaviour. The magnetic field was applied in steps of 4 kA/m to 1194 kA/m. Both the AP and AR samples have similar magnetic properties, i.e. the saturation magnetisation, remanence magnetisation and coercivity are within 5% of each other. It was thought that the AP sample would have a higher saturation magnetisation than the AR sample due to the compaction of the polymer and steel by extrusion. As this measurement is measured by weight of the sample (0.03 g) then this could mean that the composition of the polymer and steel remains unchanged from AR sample to the AP sample. The AR, AP and SS samples saturation magnetisations were measured to be 130 ± 0.15, 123 ± 0.085 and 150 ± 0.82 Am^2/kg respectively. While the remanence magnetisation for the AR, AP and SS samples were 0.56 ± 0.005, 0.588 ± 0.007 and 1.2 ± 0.01 Am^2/kg respectively and the coercivity for AR, AP and SS print were 1.27 ± 0.008, 1.33 ± 0.012 and 1.16 ± 0.012 kA/m respectively. The hysteresis loop of the SS sample showed an increase in the saturation magnetisation of 20%, and remanence of 50%, while a reduction in the coercive field of 13% compared to the AP sample, due to the reduction in the porosity and removal of the polymer. From the AP sample to the SS sample, the soft magnetic behaviour improves, as the saturation magnetisation and susceptibility increases while the coercivity decreases. This is expected as there was less non-magnetic material in the sample, therefore better domain wall motion, which decreases the coercivity. The hysteresis loops are comparable to duplex stainless steel values given in the literature [39] where the saturation magnetisation is 110 Am^2/kg, coercivity of 1.4 kA/m but a varied remanence magnetisation of between 7 and 0.75 Am^2/kg is recorded. From literature [40] it was shown that applying high temperatures (400 to 600 ^oC), increases the magnetisation by burning off the polymer. For each 10% volume of stainless steel 17/4 ph gained, there is an increase of remanence of about a factor of two. Therefore, both experimental results and literature agree that the effect of removing polymer from the AP sample increases remanence, saturation magnetisation and reduces coercivity.

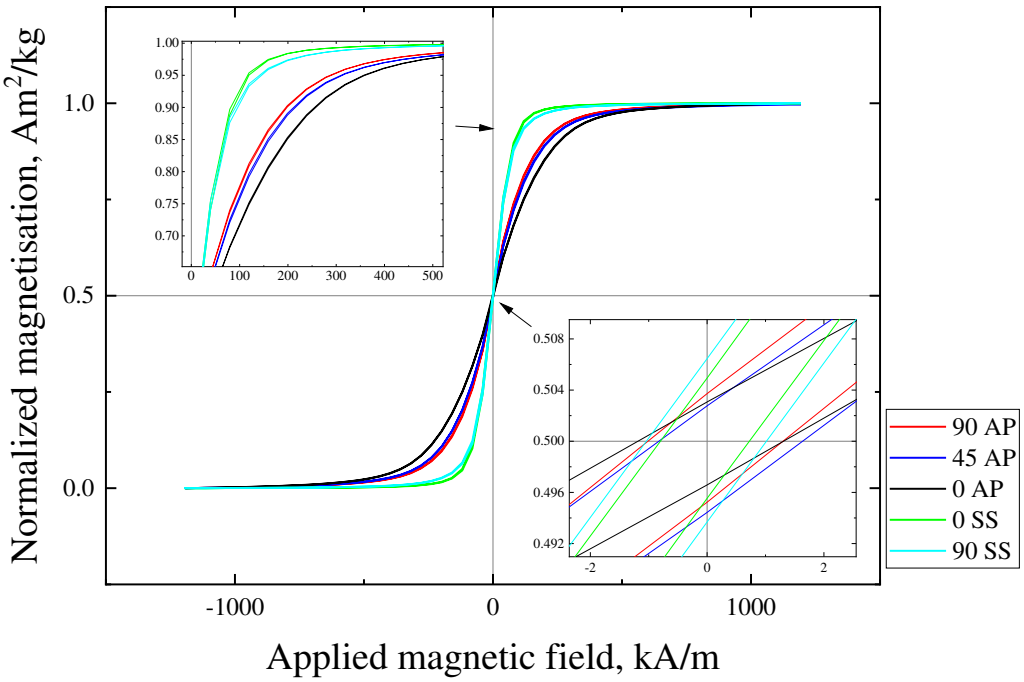

Fig. 9. Hysteresis loop measured and anisotropy is observed in 0, 45 and 90 degrees angle for AP and SS track sample - colour should be included

Fig. 9 shows the hysteresis loops for the AP and SS samples for the magnetic field parallel (0 degrees) and perpendicular (90 degrees) to the base. Anisotropy is observed in the films, as there are easy and hard axis loops. For the AP track sample at 90, 45 and 0 degrees the saturation magnetisation was 114.34 ± 0.030, 114.15 ± 0.76 and 114.52 ± 0.15 Am^2/kg respectively. For the SS track samples, the saturation magnetisation at 0 and 90 degrees was 147.83 ± 0.030 and 147.83 ± 0.094 Am^2/kg respectively. The remanence magnetisation for the AP track sample at 90, 45 and 0 degrees was 0.97 ± 0.01, 0.96 ± 0.02 and 0.75 ± 0.02 Am^2/kg, while for the SS track sample at 0 and 90 degrees, it was 1.36 ± 0.07 and 1.85 ± 0.08 Am^2/kg respectively. The magnetic coercivity for the AP track sample at 90, 45 and 0 degrees was 1.16 ± 0.02, 1.24 ± 0.04 and 1.25 ± 0.03 kA/m respectively and for the SS track sample at 0 and 90 degrees was 0.76 ± 0.04 and 1.03 ± 0.05 kA/m respectively. Fig. 9 shows soft magnetic behaviour in all directions for both samples. However, the susceptibility (gradient of the hysteresis loop through zero field) changes from 0 to 90 degrees for both the AP and SS samples. The SS sample shows softer magnetic behaviour as the coercivity reduces from the perpendicular direction to the parallel direction with respect to the field. The results for the AP track shows that there was an increase in remanence magnetisation but shows a reduction in coercivity from 0 to 90 degrees, hence the easy axis lies in the perpendicular direction to the plane. The magnetic anisotropy may be due to the printing stage where the direction of extrusion is directly perpendicular to the track plane. The change in anisotropy field, H_k, is greater from the 0 degrees to 45 degrees than from 45 degrees to the 90 degrees direction. In the paper by Watson [41], they showed that controlling the direction of deposition can influence the anisotropy within the printed sample. Therefore, as the print direction is parallel to the layers, the demagnetisation effect increases, which increases sensitivity perpendicular to the track plane. Interestingly, these results indicate additional degree of freedom in the demagnetisation effect control because by controlling print location we can control anisotropy due to porosity, as seen in SEM image (Fig. 7c).

The SS track sample shows greater isotropic magnetisation in the in-track plane, as both 90 and 0 degrees hysteresis loops have similar slope and magnetic properties. The difference in the change in coercive field and remanence magnetisation for the SS sample is larger than the AP track sample.

However, as the remanence magnetisation is larger at 90 degrees for the SS track sample, there is an increase in coercive field by 26%, which is unusual and suggest that the easy direction has switched from 90 degrees in the AP track to 0 degrees (in plane) for the SS track. This may be due to the reduction of pores and increase in grain growth in the track direction as sintering causes relief of the internal stresses. This therefore forms a homogeneous structure with greater directional magnetisation than the AP track. The uniform magnetic properties can arise due to the γ(fcc)-α(bcc) after the heat treatment [42] .

Fig. 10 shows an example of the anisotropy energy calculation. Part of the hysteresis loop and the slope from the coercivity is shown. The area of saturation magnetisation and the slope from the coercive field from each AP field direction is shown. The anisotropy energy K^1 is calculated by $K^1 = -1/2\ \Delta HB_s$ in J/m^3. Fig. 10b shows the estimated anisotropy energy K^1 of stainless steel 17/4 ph derived from the area of the slope from coercivity and saturation magnetisation in Fig 10a. The AP track in the 0, 45 and 90 degrees has anisotropy energy of -1.29 ± 0.0017, -1.28 ± 0.0085 and -0.031 ± 8.18 x 10^{-6} K^1 ($10^4 J/m^3$) respectively and SS in the 0 and 90 degrees has anisotropy energy of -1.29 ± 0.0023 and -0.98 ± 6.23 x 10^{-4} K^1 ($10^4 J/m^3$) respectively. It shows that the AP sample anisotropy energy at 90 degrees field direction, has 97.5 % less anisotropy energy compared to the field direction in 0 degrees. In comparison with the SS sample, the anisotropy energy for field direction at 90 degrees has 13.3 % less anisotropy energy than at 0 degrees. Although the AP sample has anisotropic magnetisation, the effect of heat treatment and sintering has caused the SS sample to have isotropic magnetisation. Therefore, further research is needed in post treatment such as hot isostatic pressing or magnetic field induced sintering to obtain anisotropic magnetisation within the track.

a

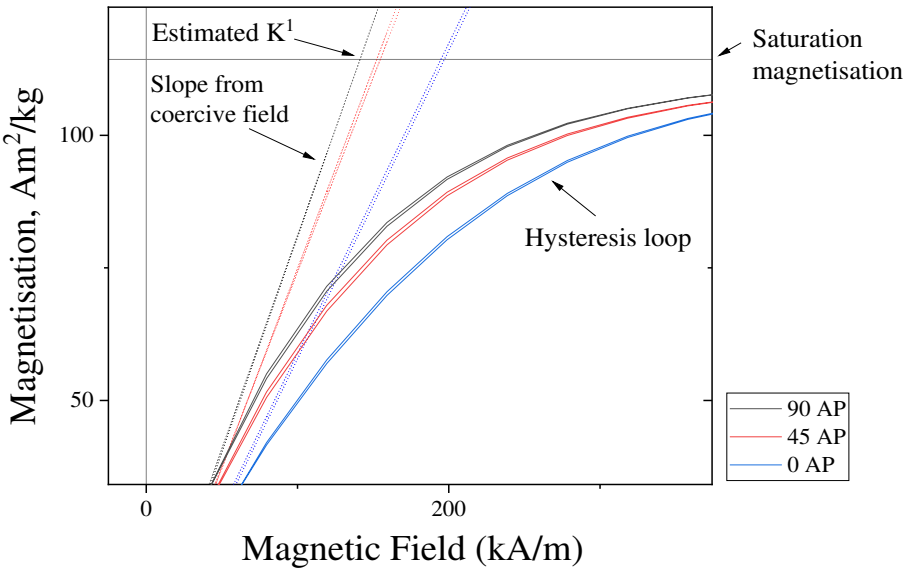

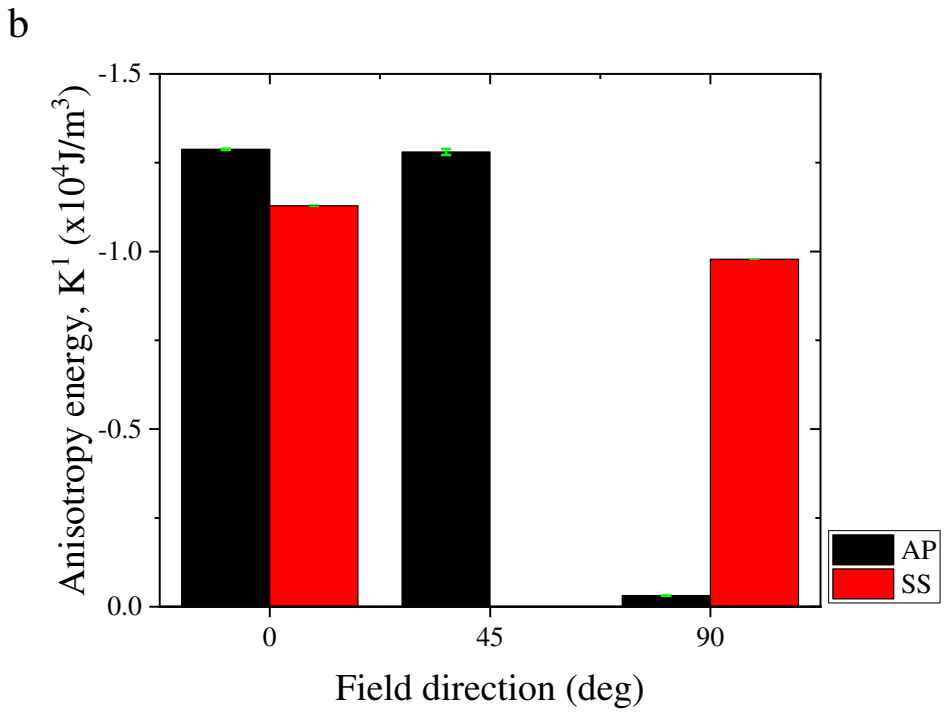

Fig. 10. (a) Estimated anisotropy energy calculation from hysteresis loop and (b) Anisotropy energy K^1 of as-printed (AP) and sintered steel (SS) in 0, 45, 90 field direction- colour should be included

4.3 Magnetostriction

The preliminary magnetostriction constant for 1 mm SS 17/4 ph was measured to be around 26 ppm in the positive field direction (Fig. 11). The martensite steel showed equiaxed grain structure in the SS part. Compared to literature, the highest magnetostriction constant for duplex steel achieved was around 18 ppm [43]. Interestingly the published value shows a sharp increase in strain and saturates around 48 kA/m whereas the 3D printed SS sample saturated around 300 kA/m. This is due to the structure of the sample, as in the literature they have used a cylinder shape where the easy axis is along the cylinder axis whereas this result has a rectangular type shape, therefore reaches saturation later due to the shape and size of the sample. However, the results do appear to be similar to the published values as most duplex steel lies between 5 ppm to 18 ppm depending on their composition and microstructure.

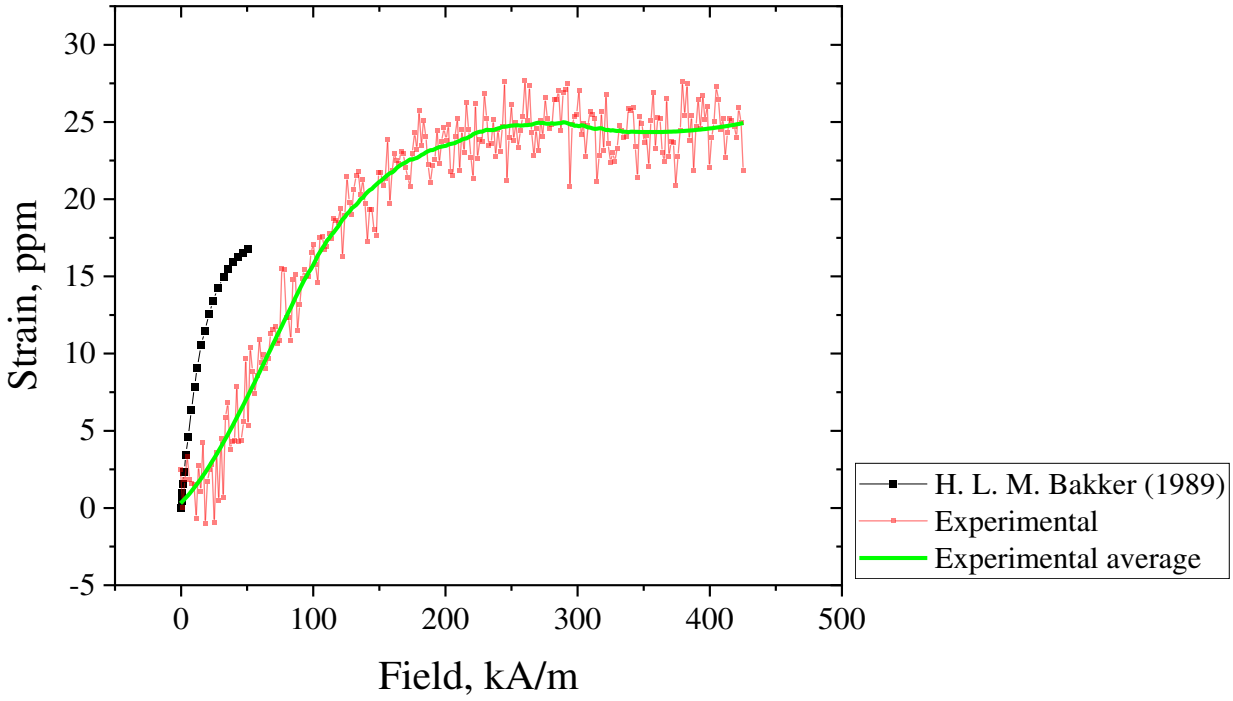

Fig 11. Comparison of duplex steel and stainless steel 17/4 ph strain as a function of field in the parallel direction - colour should be included

The magnetostriction constant for the printed grid designs was measured for the AP sample and the SS sample parallel and perpendicular to the magnetic field as seen in Fig. 12. The average data were taken for each of the data sets and presented in Fig.12. This was due to the data having a low signal to noise ratio, so taking the average allowed for the magnetostriction data to be compared easier. The SS sample shows a maximum magnetostriction constant of 26 ppm whereas compared to the AP sample of 12 ppm, parallel to the magnetic field. There is also an effect due to design, as the 3 mm SS magnetostriction is slightly lower than the 1 mm SS grid design magnetostriction. When the field is applied perpendicular to the designs, the magnetostriction constant reduces near to zero magnetostriction which is at the sensitivity level of the strain gauge.

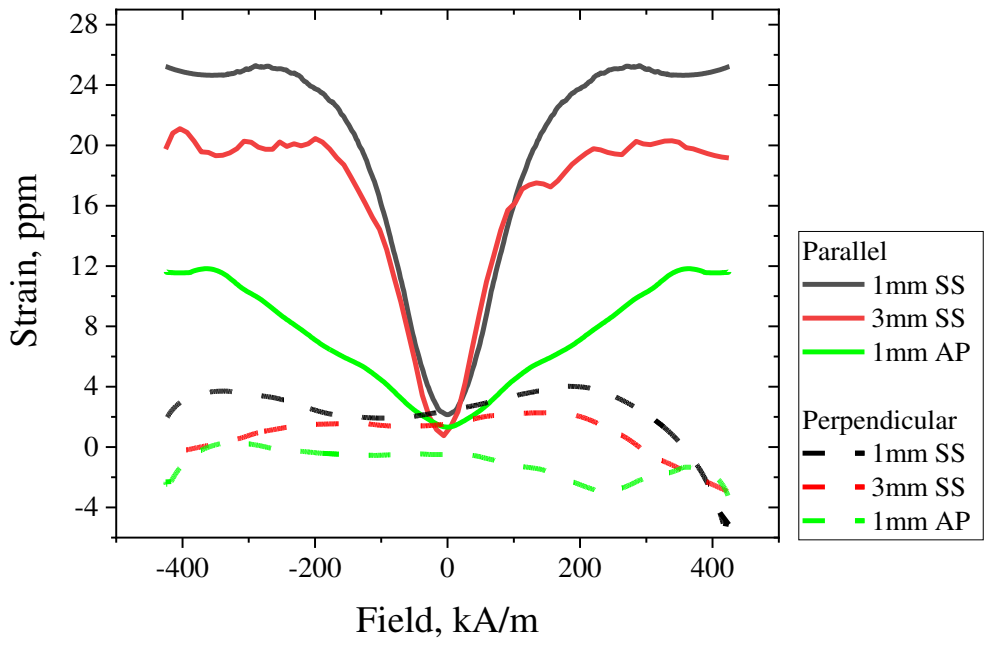

Fig. 12. SS (black and red line) and AP (green line) average magnetostriction parallel (solid line) and perpendicular (dash line) to field - colour should be included

The magnetostrictive result shown in Fig. 12 shows that the AP sample had a smaller magnetostriction constant compared to the SS sample. This is due to the presence of non-magnetic components such as polypropylene in the AP sample, that will affect the magnetostriction constant by restricting the steel domains in the parallel direction to the field. Further for the two SS samples with 1 mm and 3 mm gap, the field at which the magnetostriction becomes saturated is reduced by 50 % compared to the 1 mm AP. This is due to the magnetic domains being more free to orientate towards the field direction than the 1 mm AP sample. Furthermore, the field at which saturation magnetostriction occurs for the AP sample is at 400 kA/m which forms a broader strain/field rate. The broadening of the rate is due to the polymer binder that restricts orientation of the metal particles to align towards the field. Interestingly polymer could be used to manipulate magnetostriction either by tailoring the sintering process e.g. hot isostatic pressing or designing porous structures in the future. For the negative field, the 1 mm SS sample has a higher magnetostriction constant than the 3 mm SS sample, due to the track distance of the print, as the 1 mm track SS print reaches around 26 ppm. For the positive field, the strain for both samples reaches around 22 ppm. This may be due to the positioning of the sample print in the electromagnet as the saturation magnetostriction at a field is not the same for both sides. For example, the saturation magnetostriction is at -318 kA/m whereas the saturation at the positive field is at 400 kA/m, therefore the positive field may have not fully saturated.

Air gaps or porosity in the printing process can affect the mechanical properties such as toughness and modulus however the same is not said with magnetic properties. In [44], they explore the effects of sintering cycles and magnetostriction on cobalt ferrite nanopowders. The increase in density due to the sintering cycles was found not to be proportional to magnetostriction. However, intergranular pores had an effect on magnetostriction.

When the magnetic field is applied in the perpendicular direction to the strain gauge as seen in Fig 12, the saturation magnetostriction remains the same for both the AP and SS samples, as they are both near to zero magnetostriction. However, after plateauing the strain reduces to a negative value for both positive and negative fields at around 239 to 318 kA/m. This is more prominent in the 1 mm SS sample,

where the rate of negative magnetostriction is the highest of around -8 ppm. This may be due to the design rather than the microstructure of stainless steel 17/4 ph as the change in design from 3 mm SS sample to 1 mm SS sample increased the negative effect.

4.4 Magnetic camera

Using the magnetic camera (Magcam), the demagnetisation state of the different SS samples was investigated. It was found that the demagnetising field of the SS sample shows that there is an interesting demagnetisation arrangement of negative and positive fields out of the plane of the sample as seen in Fig. 13. For example, the 1mm track gap shows a distinct positive field however the track pattern can't be observed, whereas the 5 mm track gap shows a greater definition in field as the track pattern can be observed. The different track gaps of 1.5 mm, 3 mm and 5 mm for the SS samples all show a difference in out of plane field.

a

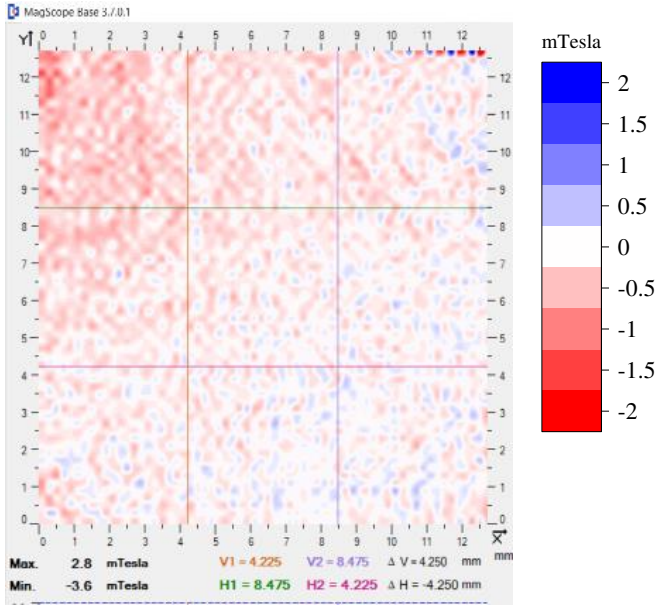

b

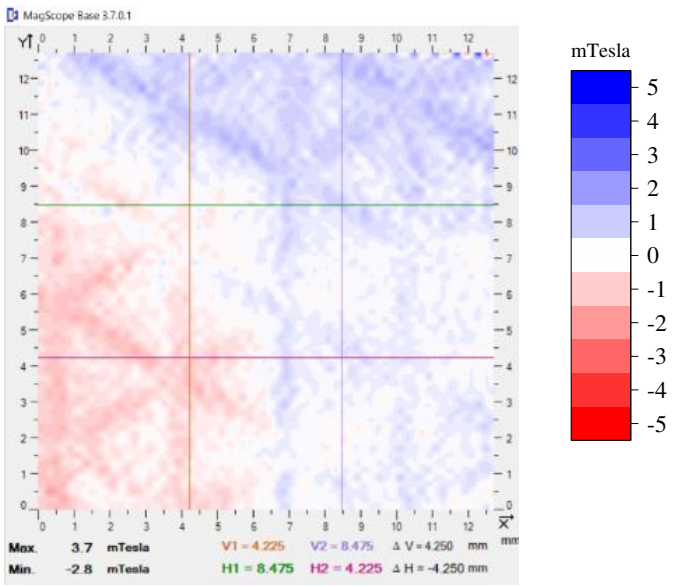

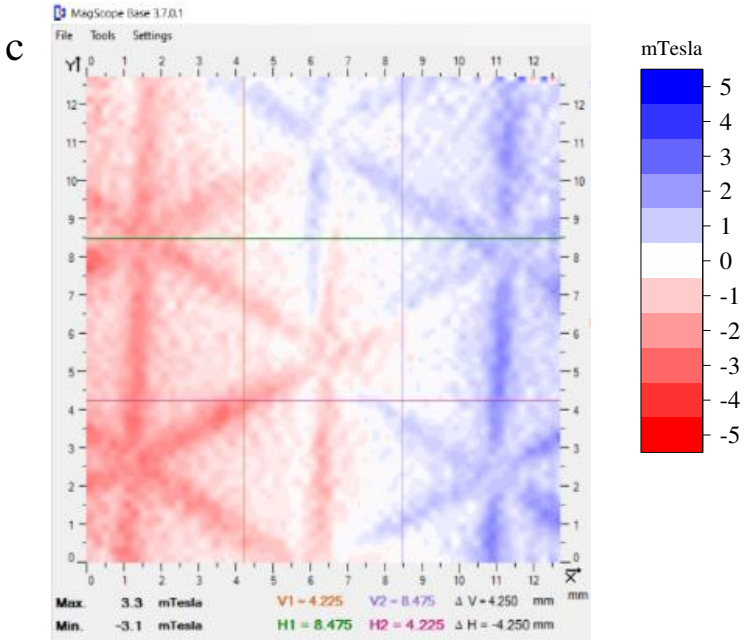

Fig. 13. Magnetic camera image measuring magnetic flux density of the SS samples with (a) 1.5 mm, (b) 3 mm and (c) 5 mm track distance - colour should be included

Fig. 13 showed that the out of plane field for each SS sample, whereas the track gap increases the greater the out of plane field difference increases. This could be due to the warping of the grid structure during heat treatment as the 5 mm grid design (c) has shown a greater heterogeneity of negative and positive out of plane field. Expansion and contraction is greater in the 5 mm SS sample therefore would form larger magnetic domains. Since heat treatment is after the sintering stage, the magnetic ordering could occur when cooling down after the sintering process below melting point (T_m) temperature, affecting the domain orientation when the sample is warped. The mixture of expansion and contraction in both X and Y direction, due to reduction of air gaps, could have caused large magnetic domains to occur and create the observed positive and negative out of plane demagnetisation fields.

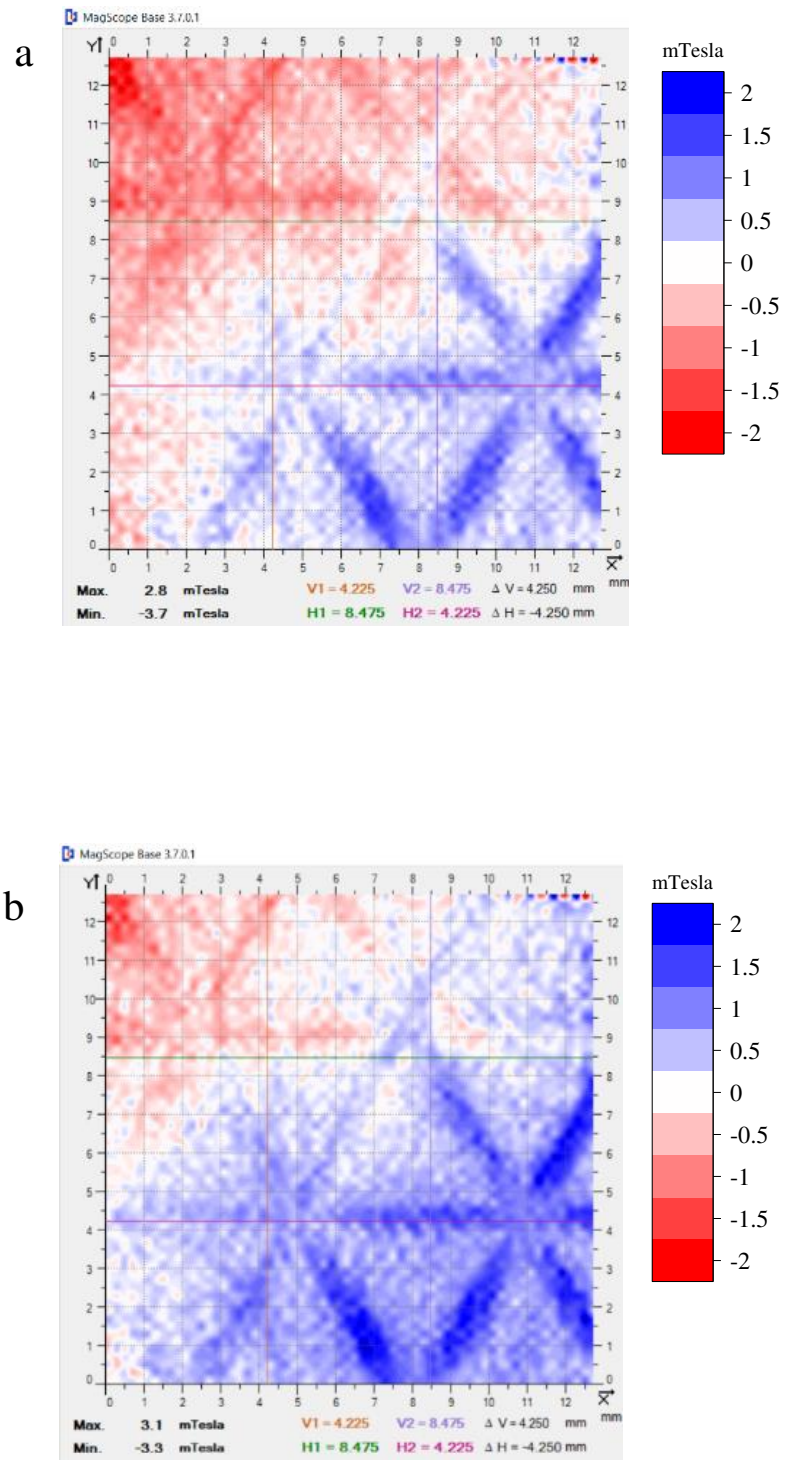

Fig. 14. Magnetic camera image measuring magnetic flux density of the SS sample with (a) 5mm track distance with no stress applied and (b) 5mm track distance with stress applied in the y direction - colour should be included

Fig. 14 shows the stress applied to the 5 mm grid sample where (a) is an image taken with no stress and (b) is where an image is taken during an applied stress with a vice in the y direction (in plane). For visibility, the field range was reduced to 2 mT. In comparison, the positive magnetic field has increased out of plane as stress is applied. This therefore shows the dynamics of Villari effect visually when

applying stress to the grid structure. Much smaller stress effect on the magnetic camera image was observed for the AP sample in agreement with its smaller magnetostriction.

5 Conclusion

To conclude, we have successfully 3D printed stainless steel 17/4 ph via DMBD printer and measured the magnetostriction property. Analysis of how the magnetostriction and magnetic properties vary in relation to the printed structure throughout the printing process was reported. The composition of steel and polypropylene present in the AR, AR and SS samples was determined using FTIR and EDX analysis. Magnetisation and anisotropy measurements showed that there is an increase in magnetisation after sintering but showed a reduction in anisotropy (K^1). The calculated anisotropy energy showed that AP sample had the largest K^1 which could be useful as a sensor or an actuator as it has an increased performance in anisotropy. The magnetic camera shows the difference in magnetic flux density on various track distances. The 5 mm track distance structure showed greater difference in positive and negative flux and larger domain sizes, which may be due to warpage during heat treatment. The SS sample had a saturation magnetostriction of around 26 ppm which was 54% more than the AP structure making the sample more sensitive to deformation. The AP strain in the parallel direction was broader and saturated at 398 kA/m whereas the SS sample saturated at 300 kA/m. Strain in the perpendicular direction showed near zero magnetostriction. Relation between density and design density at each stage of the printing process was explored in this paper. This research enhances an exciting branch of 3D printing by improving and developing AM magnetostrictive material for magnetic sensors or actuators in the future.

6 Reference

[1] K. J. Merazzo *et al.*, "Magnetic materials: a journey from finding north to an exciting printed future," *Mater. Horizons*, 2021.

[2] C. Zhang *et al.*, "3D Printing of Functional Magnetic Materials: From Design to Applications," *Adv. Funct. Mater.*, vol. 31, no. 34, Aug. 2021.

[3] V. Chaudhary, S. A. Mantri, R. V. Ramanujan, and R. Banerjee, "Additive manufacturing of magnetic materials," *Progress in Materials Science*, vol. 114. Elsevier Ltd, 01-Oct-2020.

[4] X. Wei, M. L. Jin, H. Yang, X. X. Wang, Y. Z. Long, and Z. Chen, "Advances in 3D printing of magnetic materials: Fabrication, properties, and their applications," *Journal of Advanced Ceramics*, vol. 11, no. 5. Springer, pp. 665–701, 20-Apr-2022.

[5] S. Anas Ansar, A. Singh, S. Aggrawal, N. Soni, and P. Chandra Pathak, "A Systematic Review on 4D Printing Technology," *Mater. Today Proc.*, Mar. 2023.

[6] P. Pingale, S. Dawre, V. Dhapte-Pawar, N. Dhas, and A. Rajput, "Advances in 4D printing: from stimulation to simulation," *Drug Deliv. Transl. Res.*, vol. 13, no. 1, pp. 164–188, 2023.

[7] H. W. Tan, Y. Y. C. Choong, C. N. Kuo, H. Y. Low, and C. K. Chua, "3D printed electronics: Processes, materials and future trends," *Prog. Mater. Sci.*, vol. 127, no. June 2020, p. 100945, 2022.

[8] R. Wrobel and B. Mecrow, "A Comprehensive Review of Additive Manufacturing in Construction of Electrical Machines," *IEEE Trans. Energy Convers.*, vol. 35, no. 2, pp. 1054–1064, 2020.

[9] F. S. H. B. Freeman, A. Lincoln, J. Sharp, A. Lambourne, and I. Todd, “Exploiting thermal strain to achieve an in-situ magnetically graded material,” *Mater. Des.*, vol. 161, pp. 14–21, Jan. 2019.

[10] S. Y. Chin *et al.*, “Additive manufacturing of hydrogel-based materials for next-generation implantable medical devices,” *Sci. Robot.*, vol. 2, no. 2, Jan. 2017.

[11] J. Zhang *et al.*, “3D-printed magnetic Fe3O4/MBG/PCL composite scaffolds with multifunctionality of bone regeneration, local anticancer drug delivery and hyperthermia,” *J. Mater. Chem. B*, vol. 2, no. 43, pp. 7583–7595, Oct. 2014.

[12] M. V. Patton *et al.*, “Manipulating magnetic anisotropy in fused filament fabricated parts via macroscopic shape, mesoscopic infill orientation, and infill percentage,” *Addit. Manuf.*, vol. 27, pp. 482–488, May 2019.

[13] K. Markandan and C. Q. Lai, “Fabrication, properties and applications of polymer composites additively manufactured with filler alignment control: A review,” *Compos. Part B Eng.*, vol. 256, p. 110661, May 2023.

[14] M. Lalegani Dezaki and M. Bodaghi, “Sustainable 4D printing of magneto-electroactive shape memory polymer composites,” *Int. J. Adv. Manuf. Technol.*, vol. 1, p. 3, 2023.

[15] M. J. Dapino, “On magnetostrictive materials and their use in adaptive structures,” *Struct. Eng. Mech.*, vol. 17, no. 4, 2004.

[16] Z. Leong, W. Holmes, J. Clarke, A. Padki, S. Hayes, and N. A. Morley, “Magnetostrictive Sensors for Composite Damage Detection and Wireless Structural Health Monitoring,” *IEEE Trans. Magn.*, vol. 55, no. 7, pp. 1–6, 2019.

[17] M. Bashir, S. Merryisha, P. Rajendran, and M. S. Z. Abidin, “Magnetostrictive smart materials review for morphing aircraft,” *ARPN J. Eng. Appl. Sci.*, vol. 14, no. 3, pp. 668–676, 2019.

[18] M. G. Ozden and N. A. Morley, “Laser Additive Manufacturing of Fe-Based Magnetic Amorphous Alloys,” *Magnetochemistry*, vol. 7, no. 2, p. 20, Jan. 2021.

[19] D. C. Jiles, “Recent advances and future directions in magnetic materials,” *Acta Mater.*, vol. 51, no. 19, pp. 5907–5939, Nov. 2003.

[20] D. C. Jiles, “Theory of the magnetomechanical effect,” *J. Phys. D. Appl. Phys.*, vol. 28, no. 8, pp. 1537–1546, 1995.

[21] A. Zitoun, S. Dixon, M. Kazilas, and D. Hutchins, “Defect Detection and Imaging in Composite Structures Using Magnetostrictive Patch Transducers,” *Sensors*, vol. 23, no. 2, 2023.

[22] S. Hassani and U. Dackermann, “A Systematic Review of Advanced Sensor Technologies for Non-Destructive Testing and Structural Health Monitoring,” *Sensors*, vol. 23, no. 4, 2023.

[23] D. Das *et al.*, “Circuit-Level Modeling and Simulation of Wireless Sensing and Energy Harvesting With Hybrid Magnetoelectric Antennas for Implantable Neural Devices,” *IEEE Open J. Circuits Syst.*, vol. 4, no. December 2022, pp. 139–155, 2023.

[24] D. Mukherjee and D. Mallick, “A self-biased, low-frequency, miniaturized magnetoelectric antenna for implantable medical device applications,” *Appl. Phys. Lett.*, vol. 122, no. 1, 2023.

[25] J. D. S. Vincent, M. Rodrigues, Z. Leong, and N. A. Morley, “Design and development of magnetostrictive actuators and sensors for structural health monitoring,” *Sensors (Switzerland)*, vol. 20, no. 3, p. 711, Feb. 2020.

[26] R. Carvalho *et al.*, “Improving the Performance of Paper-Based Dipole Antennas by Electromagnetic Flux Concentration,” *Cite This ACS Appl. Mater. Interfaces*, vol. 15, pp.

11234–11243, 2023.

[27] R. Brito-Pereira, C. Ribeiro, N. Pereira, S. Lanceros-Mendez, and P. Martins, “Printed multifunctional magnetically activated energy harvester with sensing capabilities,” *Nano Energy*, vol. 94, p. 106885, 2022.

[28] R. Brito-Pereira, N. Pereira, C. Ribeiro, S. Lanceros-Mendez, and P. Martins, “Environmentally friendlier wireless energy power systems: The coil on a paper approach,” *Nano Energy*, vol. 111, no. July 2022, p. 108391, 2023.

[29] A. B. Flatau, “Overview of magnetostrictive materials and their use in devices (Conference Presentation),” in *Behavior and Mechanics of Multifunctional Materials XIII*, 2019, p. 28.

[30] D. Goll *et al.*, “Additive manufacturing of soft magnetic materials and components,” *Addit. Manuf.*, vol. 27, pp. 428–439, 2019.

[31] G. Herzer, “Modern soft magnets: Amorphous and nanocrystalline materials,” *Acta Mater.*, vol. 61, no. 3, pp. 718–734, Feb. 2013.

[32] H. Schönrath *et al.*, “Additive manufacturing of soft magnetic permalloy from Fe and Ni powders: Control of magnetic anisotropy,” *J. Magn. Magn. Mater.*, vol. 478, pp. 274–278, May 2019.

[33] X. Yang *et al.*, “Effect of remelting on microstructure and magnetic properties of Fe-Co-based alloys produced by laser additive manufacturing,” *J. Phys. Chem. Solids*, vol. 130, pp. 210–216, Jul. 2019.

[34] K. Nakajima *et al.*, “Additive Manufacturing of Magnetostrictive Fe–Co Alloys,” *Materials (Basel).*, vol. 15, no. 3, Feb. 2022.

[35] C. Gao, X. Yao, Y. Deng, H. Pan, and C. Shuai, “Laser-beam powder bed fusion followed by annealing with stress: A promising route for magnetostrictive improvement of polycrystalline Fe81Ga19 alloys,” *Addit. Manuf.*, vol. 68, no. July 2022, p. 103516, 2023.

[36] A. P. Nandakumar, “Low Cost Metal Additive Manufacturing by Extrusion using Metal Injection Moulding Principles,” 2019.

[37] M. R. Jung *et al.*, “Validation of ATR FT-IR to identify polymers of plastic marine debris, including those ingested by marine organisms,” *Mar. Pollut. Bull.*, vol. 127, pp. 704–716, 2018.

[38] Desktop Metal, “17-4 PH stainless steel data sheet,” 2018. [Online]. Available: https://www.desktopmetal.com/uploads/Studio-MDS-17-4-PH-stainless-steel.pdf.

[39] K. P. Davidson and S. Singamneni, “Magnetic Characterization of Selective Laser-Melted Saf 2507 Duplex Stainless Steel,” *JOM*, vol. 69, no. 3, pp. 569–574, Mar. 2017.

[40] B. Khatri, K. Lappe, D. Noetzel, K. Pursche, and T. Hanemann, “A 3D-printable polymer-metal soft-magnetic functional composite-development and characterization,” *Materials (Basel).*, vol. 11, no. 2, 2018.

[41] N. D. Watson and P. von Lockette, “Deposition controlled magnetic alignment in iron-PLA composites,” in *Solid Freeform Fabrication 2018: Proceedings of the 29th Annual International Solid Freeform Fabrication Symposium - An Additive Manufacturing Conference, SFF 2018*, 2020, pp. 1145–1151.

[42] A. Stashkov *et al.*, “Magnetic, electric properties and hardness of 17-4 PH stainless steel fabricated by selective laser melting,” in *Journal of Physics: Conference Series*, 2019, vol. 1389, no. 1, p. 12124.

[43] H. L. M. Bakker, “Magnetostriction of duplex stainless steels,” *Mater. Sci. Technol. (United*

Kingdom), vol. 5, no. 11, pp. 1135–1139, Jan. 1989.

[44] K. K. Mohaideen and P. A. Joy, “Studies on the effect of sintering conditions on the magnetostriction characteristics of cobalt ferrite derived from nanocrystalline powders,” *J. Eur. Ceram. Soc.*, vol. 34, pp. 677–686, 2014.

7 Acknowledgement

This research was funded under the DSTL Anglo-French studentship scheme and the Henry Royce Institute for Advanced Materials, funded through EPSRC grants EP/R00661X/1, EP/S019367/1, EP/P02470X/1 and EP/P025285/1, for the desktop printer and SQUID access at The University of Sheffield. Magnetostriction measurements was performed at IPCMS.